Antenna Calibration for Near-Field Material Characterization

Greg Hislop, *Senior Member, IEEE*, Christophe Craeye, *Senior Member, IEEE*, and David González Ovejero, *Member, IEEE*

***Abstract*—A novel antenna calibration method is presented for near-field problems, such as material characterization or inverse scattering. The procedure accurately accounts for differences between simulations of objects close to antennas and the equivalent experimental measurements. It is based on the method of moments (MoM) solution to surface integral scattering equations. An efficient choice of macrobasis functions (MBFs) is applied to the antenna, which reduces the computational costs by several orders of magnitude. The calibration involves scanning a target of known constitution through the antenna near field, assigning a tuning parameter to each MBF and optimizing said parameters, so as to reduce the error between antenna simulations and measurements. This adjusts the antenna's simulated surface currents, so as to more accurately represent the currents on the experimental apparatus. Thus, an efficient antenna model is obtained, which more accurately represents the real-world antenna. The calibration technique is verified by applying it to the characterization of dielectric objects of known but arbitrary shape.**

***Index Terms*—Calibration, computational electromagnetic, dielectric constant, electromagnetic tomography, electromagnetics, inverse problems, materials' testing, microwave measurements, microwave sensors, near fields, near-field radiation pattern, numerical simulation, permittivity measurement.**

I. Introduction

IN NEAR-FIELD imaging or sensing problems (e.g., tomography [1]–[6], material characterization [7]–[12], medical imaging [13]–[16], etc.) the interactions between the probing antenna and object under test (OUT) are complex in nature. The ideal system model includes a full-wave simulation of the probing antenna/OUT and all interactions there between [6], [17]. Imaging and sensing techniques often attempt to minimize a cost function as a function of parameters to be estimated. As such the scattering problem is solved numerous times while trialling different prospective parameter values (see [4]). This requires the antenna/OUT combination to be simulated numerous times prior to obtaining desired results. Thus, the use of computationally costly full-wave simulations may make the techniques unpractical. For this reason, most near-field problems use non-full-wave antenna representations. Indeed, antennas are often represented using significant simplifications, e.g., as point sources [2], [4], [18], Hertzian dipoles [5], transmission line equivalents [19], and finding simple ratios between simulations and measurements of the antenna(s) in free space (or with a calibration target) and multiplying all future simulations by these ratios [20], assuming that the antenna response is a simple convolution between a point spread function and the OUT [21] or including only elementary antenna parameters such as beamwidth, gain [22], etc. One may decrease coupling and multiple interactions between antennas and OUT by using lossy matching liquids but this also deceases the signal-to-noise ratio (SNR) [16].

The technique proposed in this paper makes use of the method of moments (MoM) for surface integral scattering equations as the means of simulating the probing antenna [23]–[26]. Normally, this would contribute an unacceptable additional computational load; however, the technique here described reduces said load to be well and truly below that required to simulate the OUT. Macrobasis functions (MBFs) are chosen via a calibration technique and employed, this allows surface currents to be represented by a small set of vectors each representing a possible current distribution across the entire surface rather than many small basis functions [27]–[29]. This calibration uses antenna simulations to choose and reduce the number of MBFs by requiring accurate simulation of fields radiated in the direction of any potential OUT, while accepting the possibility of a lower quality representation of fields radiating in other directions. In this way, the computational cost of including the full-wave antenna simulation in the sensing problem is reduced by several orders of magnitude.

It is well known that even quasi-exact full-wave simulations of antennas (e.g., with MoM or FDTD) differ from measurements taken with the real-world manufactured system. This is due to manufacturing tolerances, positioning/pointing errors, meshing inaccuracies, inaccuracies in the feed port model, etc. As these differences between real-world and simulated systems are difficult to identify, it is important to employ an antenna calibration technique when using simulations as the forward modeling component of a sensing or imaging problem. Many such calibration methods exist that take various antenna characteristics into account (e.g., [19], [22]). The technique

Manuscript received June 22, 2015; revised November 30, 2015; accepted January 10, 2016. Date of publication February 05, 2016; date of current version April 05, 2016. This work was supported by the Belgian "Fonds National de la Recherche Scientifique (FNRS)" under the CARASCAT project.

G. Hislop was with the Institute of Information and Communication Technologies, Electronics and Applied Mathematics (ICTEAM), Université catholique de Louvain (UCL), Louvain-la-Neuve 1348, Belgium. He is now with the Fugro-Roames, Brisbane, QLD 4113, Australia (e-mail: gregory.hislop@gmail.com).

C. Craeye is with the Institute of Information and Communication Technologies, Electronics and Applied Mathematics (ICTEAM), Université catholique de Louvain (UCL), Louvain-la-Neuve 1348, Belgium (e-mail: christophe.craeye@uclouvain.be).

D. G. Ovejero was with the Institute of Information and Communication Technologies, Electronics and Applied Mathematics (ICTEAM), Université catholique de Louvain (UCL), Louvain-la-Neuve 1348, Belgium. He is now with the Jet Propulsion Laboratory, California Institute of Technology, Pasadena, CA 91125 USA.

Digital Object Identifier 10.1109/TAP.2016.2526087

proposed here is, however, to the authors' knowledge, the first to incorporate a full-wave simulation of the antenna–OUT interactions without significantly increasing the computational load. It functions through the use of a small number of tuning parameters that, in conjunction with calibration measurements, alter the space of antenna surface currents represented via the set of selected MBF vectors, so as to incorporate the differences between the real-world antenna and the MoM model thereof.

The result is an extremely efficient antenna simulation which via calibration caters for unknown differences between the real-world and modeled antennas. This paper validates the calibration technique by applying it to the problem of complex permittivity estimation of an OUT of known shape but unknown material characteristic. This novel material characterization method is a secondary contribution of this paper at hand. Detailed results on both simulated and experimental data show that the calibration method accurately represents the feed current of an antenna, and accurate permittivity estimation shows the calibration's practical usefulness in near-field problems.

An existing work [6] incorporates antennas into a microwave tomography problem in a similar way as this paper at hand. However, the new work improves on the old by intelligently choosing MBFs to reduce the computational load and to enable antenna calibration. This paper [17] obtains accurate simulations of experimental feed currents for a near-field monopole array with the finite-element method; however, unlike the work at hand, they must include the full computational cost of the antenna-to-OUT interactions each time the OUT changes and do not possess a calibration process.

The material characterization problem tackled in this paper may be viewed as a simplified form of the multistatic tomographic or inverse scattering problem currently of interest to the microwave medical imaging community. The proposed calibration could also be used for such problems [1]–[4], [13]–[16].

The concepts in this paper were briefly introduced with limited preliminary results in [11], [30]. This paper presents the concept in detail with extensive quality results. This paper starts with Section II that presents the mathematical theory behind the problem. The governing MoM formulation, the calibration, and parameter measurement procedures are described in Sections II-A–II-C, respectively. The experimental procedure is outlined in Section III, the detailed simulation-based results are given in Section IV, with the experimental results in Section V. A discussion is given in Section VI and Section VII concludes this paper.

II. Mathematical Formulation

A. Governing MoM Equations

The surface integral MoM matrix equation for a dielectric in the presence of an antenna may be represented as [6], [23]–[26]

$$\begin{bmatrix} \boldsymbol{Z}_{11}, & \boldsymbol{Z}_{12} \\ \boldsymbol{Z}_{12}^{T}, & \boldsymbol{Z}_{22} \end{bmatrix} \begin{bmatrix} \boldsymbol{x}_1 \\ \boldsymbol{x}_2 \end{bmatrix} = \begin{bmatrix} \boldsymbol{v}_1 \\ \boldsymbol{v}_2 \end{bmatrix} \tag{1}$$

where $\boldsymbol{Z}_{11}$ is an $N \times N$ MoM matrix of reaction integrals between the N elementary basis/testing functions (Rao–Wilton–Glisson (RWG) [31]) used to discretize the antenna, $\boldsymbol{Z}_{22}$ is a $B \times B$ MoM matrix of the interactions between the B RWG elementary basis/testing functions representing the OUT (i.e., the calibration target or the sample to be measured) and $\boldsymbol{Z}_{12}$ is an $N \times B$ MoM matrix of the reaction integrals between the N basis functions of the antenna and the B elementary testing functions of the OUT. The vectors $\boldsymbol{x}_1$ and $\boldsymbol{x}_2$ contain the coefficients, which are multiplied by their corresponding basis functions, form the surface current densities on the antenna and OUT, respectively. The excitation vectors $\boldsymbol{v}_1$ and $\boldsymbol{v}_2$ represent the voltage densities applied to the antenna and OUT, respectively. The matrix transpose is denoted by ^{T}.

A directional ultra-wideband (UWB) antenna is used to direct radiation toward the target and to facilitate measurements across a wide bandwidth. Such antennas are electrically large making $\boldsymbol{Z}_{11}$ and $\boldsymbol{Z}_{12}$ large. To reduce the computational complexity of the problem, an MBF representation of the antenna is used [27]–[29]. MBFs reduce the size of MoM matrices (and thus the computational cost) by representing the surface current density with a small set of $M << N$ distributions each covering the entire antenna surface as opposed to assigning an unknown to each of N local-domain basis functions. Letting M MBFs form the columns of the MBF matrix $\boldsymbol{Q}$, the current density on the antenna can be represented as

$$\boldsymbol{x}_1 = \boldsymbol{Q}\boldsymbol{x}_{mbf}. \tag{2}$$

Applying this definition and left multiplying the upper set of equations in (1) by $\boldsymbol{Q}^T$ (Galerkin testing) gives

$$\begin{bmatrix} \boldsymbol{Q}^T\boldsymbol{Z}_{11}\boldsymbol{Q}, & \boldsymbol{Q}^T\boldsymbol{Z}_{12} \\ \boldsymbol{Z}_{12}^{T}\boldsymbol{Q}, & \boldsymbol{Z}_{22} \end{bmatrix} \begin{bmatrix} \boldsymbol{x}_{mbf} \\ \boldsymbol{x}_2 \end{bmatrix} = \begin{bmatrix} \boldsymbol{Q}^T\boldsymbol{v}_1 \\ \boldsymbol{v}_2 \end{bmatrix}. \tag{3}$$

The MBF selection procedure is described in Section II-B. In (3), $\boldsymbol{Q}^T\boldsymbol{v}_1$ represents the voltage density applied across the antenna using a linear summation of MBFs, $\boldsymbol{x}_{mbf}$ is the equivalent MBF representation of the current densities formed due to the applied voltages, and the MoM matrix represents the relationship between these values when the antenna is in the presence of the OUT.

No matter how much care is taken in the design, manufacture, and mounting of the antenna, the response of the experimental apparatus will always differ (even if only slightly) from its MoM simulation. Such differences can have a significant negative effect on the results of an inverse near-field problem. Thus, a calibration procedure is proposed, which slightly distorts the MBF representation of the current densities [the $\boldsymbol{Q}$ matrices in (3) to the right of their corresponding impedance matrix components], so as to better represent the current densities on the real-world antenna. This paper proposes to perform this calibration by multiplying each of the MBFs in $\boldsymbol{Q}$ by a different complex scalar, the full set of which forms the vector $\boldsymbol{k}$. One may define $.*$ as the matrix element-by-element product and $\boldsymbol{1}_{a,b}$ as a matrix of size a by b with all elements equal to one. Thus, the calibration vector $\boldsymbol{k}$ is applied to (3) by replacing the $\boldsymbol{Q}$ matrices that correspond to the current density MBFs with $\boldsymbol{Q}.*(\boldsymbol{1}_{N,1}\boldsymbol{k}^T)$. Note that, $\boldsymbol{Q}$ is not scaled when appearing as a left-hand multiplication of the upper set of equations in (3) or in either the current or voltage density vectors. This procedure followed by some elementary matrix manipulations transforms (3) into

$$\begin{bmatrix} \left(\boldsymbol{Q}^T \boldsymbol{Z}_{11} \boldsymbol{Q}\right) .* \left(\mathbf{1}_{M,1} \boldsymbol{k}^T\right), & \boldsymbol{Q}^T \boldsymbol{Z}_{12} \\ \left(\mathbf{1}_{B,1} \boldsymbol{k}^T\right) .* \left(\boldsymbol{Z}_{12}^T \boldsymbol{Q}\right), & \boldsymbol{Z}_{22} \end{bmatrix} \begin{bmatrix} \boldsymbol{x}_{mbf} \\ \boldsymbol{x}_2 \end{bmatrix} = \begin{bmatrix} \boldsymbol{Q}^T \boldsymbol{v}_1 \\ \boldsymbol{v}_2 \end{bmatrix}. \quad (4)$$

Thus, the vector $\boldsymbol{k}$ is used to slightly deform the MBF representation of the antenna's current densities in such a way as to account for small differences between these current densities and those on the real-world antenna (Section II-B presents this procedure in detail).

No voltage is applied to the OUT (i.e., $\boldsymbol{v}_2 = \mathbf{0}$) and the excitation vector, relating to the antenna $\boldsymbol{v}_1$, is zero except at the feed point where an applied voltage of 1 V is assumed. The current at the feed point is obtained as

$$y = w \boldsymbol{q}_f \boldsymbol{x}_{mbf} \quad (5)$$

where $\boldsymbol{q}_f$ is the row of $\boldsymbol{Q}$ corresponding to the basis function at the feed point and w is the width of said basis function. The use of this information with the Schur complement allows (4) to be simplified to give y as

$$y = w^2 \boldsymbol{q}_f \left(\left(\mathbf{1}_{M,1} \boldsymbol{k}^T\right) .* \left(\boldsymbol{Q}^T \boldsymbol{Z}_{11} \boldsymbol{Q} - \boldsymbol{Q}^T \boldsymbol{Z}_{12} \boldsymbol{Z}_{22}^{-1} \boldsymbol{Z}_{12}^T \boldsymbol{Q}\right)\right)^{-1} \boldsymbol{q}_f^T. \quad (6)$$

Note that, the feed current obtained in the absence of the OUT (i.e., in free space) is

$$\tilde{y} = w^2 \boldsymbol{q}_f \left(\left(\mathbf{1}_{M,1} \boldsymbol{k}^T\right) .* \left(\boldsymbol{Q}^T \boldsymbol{Z}_{11} \boldsymbol{Q}\right)\right)^{-1} \boldsymbol{q}_f^T \quad (7)$$

and that for any nonsingular square matrix $\boldsymbol{P}$

$$\left(\left(\mathbf{1}_{M,1} \boldsymbol{k}^T\right) .* \boldsymbol{P}\right)^{-1} = \left(1./\left(\boldsymbol{k} \mathbf{1}_{1,M}\right)\right) .* \boldsymbol{P}^{-1} \quad (8)$$

where ./ represents an element by element division. Thus, one may define the difference current Δy as being

$$\Delta y = y - \tilde{y} = w^2 \left(\boldsymbol{q}_f ./ \boldsymbol{k}^T\right) \left(\left(\boldsymbol{Q}^T \boldsymbol{Z}_{11} \boldsymbol{Q} - \boldsymbol{Q}^T \boldsymbol{Z}_{12} \boldsymbol{Z}_{22}^{-1} \boldsymbol{Z}_{12}^T \boldsymbol{Q}\right)^{-1} - \left(\boldsymbol{Q}^T \boldsymbol{Z}_{11} \boldsymbol{Q}\right)^{-1} \right) \boldsymbol{q}_f^T. \quad (9)$$

B. Calibration Procedure

Equation (9) represents the MBF reduced and calibrated MoM simulation of the difference current in the presence of an OUT. A three-step calibration needs to be performed before (9) may be used as part of a near-field sensing procedure. First, a mathematical link between the S_{11} measurement at the calibration point of the VNA and y, the theoretical current at the feed basis function, needs to be established; second, the MBFs $\boldsymbol{Q}$ have to be chosen; and third, the calibration vector $\boldsymbol{k}$ must be obtained.

Step 1) The connection between the calibration point of the VNA and the feed point of the antenna is assumed to be a lossless $Z_0 = 50\ \Omega$ transmission line of length L. Its one-way phase shift is denoted by ϕ. Thus, the S_{11} value at the feed basis/testing function is as a function of the S_{11} parameter at the calibration point of the VNA [32]

$$S_{11}^f = S_{11}^{VNA} e^{j2\phi} \quad (10)$$

while the current is [32]

$$y = \frac{1 - S_{11}^f}{(1 + S_{11}^f) Z_0}. \quad (11)$$

The phase ϕ must be obtained. Thus, one simulates y via (1) and experimentally measures S_{11}^{VNA} for the antenna in free space. Equations (10) and (11) are then used to obtain $\hat{y}(\phi)$, an estimate of y from S_{11}^{VNA}. The value of ϕ minimizing the error $|y - \hat{y}(\phi)|^2$ is taken as the transmission line's phase delay. At anyone frequency, multiple minimums will exist, with the correct one being that which results in a nearly constant value of the equivalent cable length (in cm) across frequency.

Step 2) The proposed MBF selection procedure is designed to provide accurate electromagnetic simulation of waves incident from the direction of the OUT. Other directions are ignored, so as to minimize the number of MBFs M and thus reduce computational complexity. A PEC calibration target is scanned through the region that will contain the unknown object to be measured. For each of the C positions of the calibration target, the full MoM problem (1) is solved and the current densities $\boldsymbol{x}_1$ obtained across the antenna structure. These current density vectors $\boldsymbol{x}_1$ form the C columns of the temporary matrix $\boldsymbol{A}$. The SVD decomposition is then used to construct $\boldsymbol{Q}$ by keeping only the M most significant singular vectors of $\boldsymbol{A}$ [33], [34]. In such a way, the M columns of $\boldsymbol{Q}$ are orthogonal and essentially span the space of all the $\boldsymbol{x}_1$ simulated when scanning the calibration target. Thus, this small MBF space is able to accurately represent antenna surface currents induced or producing fields' incident on any target lying in a direction spanned by the C calibration measurements. For sources outside this calibrated set of directions, accuracy will be lost. When choosing the calibration target's shape, size, and C positions, it is important to ensure that the C calibration experiments incorporate radiation from all directions that may be significant to the plane-wave scattering spectrum of any eventual OUT. In practice, this may be done by scanning a small but highly reflecting target through a dense grid representing the maximum extent of an OUT.

Step 3) For a given position of the calibration target, $\boldsymbol{k}$ is the only unknown in (9). Grouping the known terms in (9) allows the equation to be represented as an efficient, linear equation in M unknowns

$$\Delta y(\boldsymbol{k}) = \sum_{a=1}^{M} \frac{s_a}{k_a} \quad (12)$$

where k_a is the ath element of $\boldsymbol{k}$ and represents the unknowns to be found by the calibration procedure and s_a is the known constant

$$s_a = w^2 \left(\hat{e}_a .* \boldsymbol{q}_f\right) \left(\left(\boldsymbol{Q}^T \boldsymbol{Z}_{11} \boldsymbol{Q} - \boldsymbol{Q}^T \boldsymbol{Z}_{12} \boldsymbol{Z}_{22}^{-1} \boldsymbol{Z}_{12}^T \boldsymbol{Q}\right)^{-1} - \left(\boldsymbol{Q}^T \boldsymbol{Z}_{11} \boldsymbol{Q}\right)^{-1} \right) \boldsymbol{q}_f^T \quad (13)$$

with $\hat{\boldsymbol{e}}_a$ unity at its ath element and zero elsewhere. Using the index i to identify individual calibration measurements and defining Δy_i^m and $\Delta y_i(\boldsymbol{k})$ as the experimentally measured and simulated difference-currents, respectively, the calibration procedure involves finding $\boldsymbol{k}$, which minimizes the root-mean-square (rms) error

$$\sqrt{\sum_{i=1}^{C} |\Delta y_i^m - \Delta y_i(\boldsymbol{k})|^2}. \tag{14}$$

As (12) is linear in nature (14) is easily minimized via Gauss's least-squares analysis.

C. Inversion of Constitutive Parameters

Constitutive parameters (e.g., complex permittivity $\varepsilon = \varepsilon_r\varepsilon_0$ and/or permeability $\mu = \mu_r\mu_0$) of an OUT, with known shapes/volume boundary locations, may now be estimated by iteratively changing parameter values in the calculation of $\boldsymbol{Z}_{22}$ in (9), so as to minimize the difference between Δy and experimentally measured feed currents. With the calibration procedure defined, (9) may be simplified by defining $\boldsymbol{p} = w^2\boldsymbol{q}_f./\boldsymbol{k}^T$, $\boldsymbol{B} = \boldsymbol{Q}^T\boldsymbol{Z}_{11}\boldsymbol{Q}$, $\boldsymbol{C} = \boldsymbol{Q}^T\boldsymbol{Z}_{12}$, and $W = \boldsymbol{p}\boldsymbol{B}^{-1}\boldsymbol{q}_f^T$ to give

$$\Delta y = \boldsymbol{p}\left(\left(\boldsymbol{B} - \boldsymbol{C}\boldsymbol{Z}_{22}^{-1}\boldsymbol{C}^T\right)^{-1}\right)\boldsymbol{q}_f^T - W. \tag{15}$$

Since the OUT's shape and location are known, the only element of (15) that cannot be precalculated is the OUT's MoM matrix $\boldsymbol{Z}_{22}$ (note that, $\boldsymbol{Z}_{12}$ is a function of the shapes of the antenna and OUT but is independent of the OUT's material properties). The use of an MBF representation of the antenna significantly reduces the computational cost of evaluating (15). Indeed, only the evaluation and inversion (or equivalent operation) of $\boldsymbol{Z}_{22}$ provide a significant numerical cost. This computational burden is significantly reduced by the use of the authors' FMIR–MoM technique [26], [35], which is able to efficiently generate MoM matrices while sweeping through complex permittivity, permeability, or frequency with a fixed object discretization. Thus, (15) is efficient to calculate and may form the core of an iterative procedure in which ε and/or μ of the OUT is changed at each iteration (it should be noted, however, that this paper does not address the measurement of permeability).

The OUT is placed in the region previously occupied by the calibration target, and is scanned through a small number of positions and/or orientations D. The frequency-dependent ε is obtained, which minimizes

$$\sqrt{\sum_{i=1}^{D} |\Delta y_i^m - \Delta y_i(f,\varepsilon)|^2} \tag{16}$$

where Δy_i^m and $\Delta y_i(f,\varepsilon)$ are, respectively, the measured and simulated [from (15)] versions of the difference current. The experiments performed in this paper exhibited no false minima and as such a local optimization technique (MATLAB's fminsearch procedure that implements the Nelder–Mead simplex method [36]) was used to minimize (16).

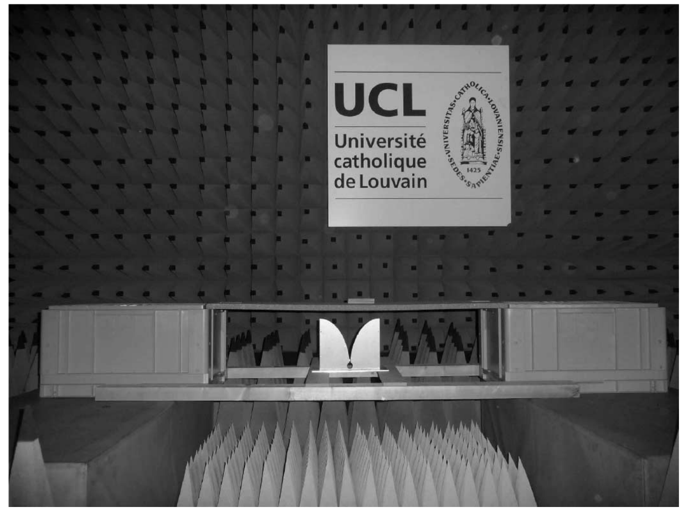

Fig. 1. Experimental setup with a wooden frame supporting the antenna, while plastic boxes support a microwave foam on which the calibration target and OUT may be positioned (the dielectric test object is present in the photo).

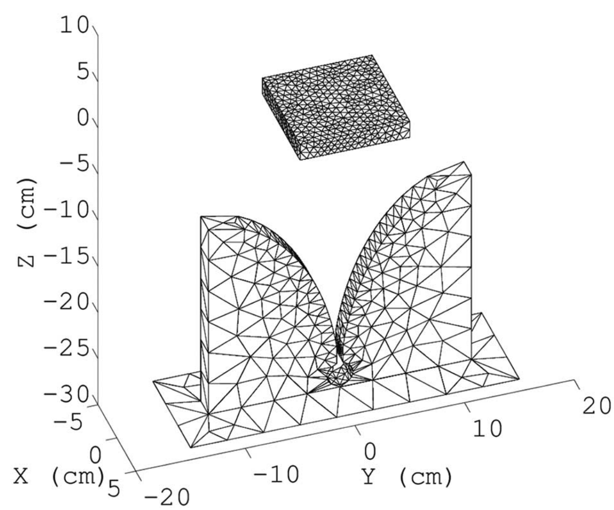

Fig. 2. MoM mesh of antenna and dielectric block.

III. Experimental Procedure

This section details the experimental apparatus and the tests performed. The apparatus is elementary, consisting simply of a single VNA port connected to an antenna mounted in an anechoic chamber (see Fig. 1, if sufficient free space is present around the experiment, time gating could be used instead of an anechoic chamber). Microwave foam ($\varepsilon \approx \varepsilon_0$, $\mu = \mu_0$) is used to mount the OUT. The antenna needs to be directive, to have a wide bandwidth and to have an MoM model that accurately simulates the experimental measurements. The authors have chosen to use a machine milled 3-D Vivaldi antenna with internal coaxial feed and no balun, which was originally designed for ground penetrating radar (GPR) applications [37], [38]. The antenna operates ($S_{11} < -10$ dB) from approximately 800 MHz to 3.6 GHz, it is directive and its MoM simulations closely match experimentation [26], [38]. The antenna has total dimensions of 30 cm × 10 cm × 20 cm and is represented by an MoM mesh made of $N = 1585$ basis functions (see Fig. 2).

The calibration target was chosen to be a thin (1-mm thick) square metal plate with 7.5-cm sides. It was scanned through $C = 52$ positions within a horizontal surface of 20 cm × 30 cm at a height of 8.7 cm from the top of the antenna. The calibration procedure was then performed as per Section II-B. Note that, the antenna is symmetric across the y-axis and thus each of the 52 measurements is identical to another measurement in the set. This allows for an estimate of the measurement error by calculating the RMS error between the theoretically identical measurements.

The test target consisted of a 10 cm × 10 cm × 1.6 cm low-loss dielectric block fabricated by Neltec and possessing a manufacturer stated frequency stable relative permittivity of $\Re(\varepsilon_r) = 2.98$ and $\Im(\varepsilon_r) < 0.005$ ($\Re(\ldots)$ and $\Im(\ldots)$ represent real and imaginary parts, respectively). A ground truth permittivity measurement was made using a VNA and truncated coaxial line as a contact probe.

The target under test was scanned through $D = 10$ positions within the calibrated space. The complex permittivity was then estimated using the procedure of Section II-C. All tests were performed independently at 15 linearly spaced frequency points starting at 800 MHz and stopping at 3.6 GHz. The initial guess for the permittivity was $\varepsilon_r = 1.5 - 1.5j$ at the lowest frequency, while for higher frequencies, the value obtained at the previously evaluated frequency was used. Fig. 2 depicts the MoM mesh of the antenna and dielectric to be measured.

Section IV will now present the results using simulated data that model the given apparatus before Section V presents the experimental results.

IV. Results Based on Synthetic Tests

This section uses the simulated data on several different target types to verify the validity of the calibration and permittivity estimation techniques and to identify some limitations. The full MoM solution, i.e., (1) was used to generate the test data. So as to avoid (or at least decrease the effect of) the "inverse crime" [39] and to introduce some modeling errors, higher density antenna and target meshes were used when generating the input data than for the inverse scattering algorithm. An additional difference between the so-called "measured" and simulated data was introduced by adding zero-mean Gaussian noise at an SNR of 60 dB (the maximum of all signal values divided by the rms of the noise) to the simulated data (this corresponds roughly to the noise floor in the experimental tests of Section V). In this way, an initial verification of the calibration and permittivity measurement process could be performed using only simulated data.

The calibration was performed using simulations of the procedure in Section III. The same calibration was used for all the simulated data tests. Initially, a simulation of a bloc of the shape of the Neltec dielectric (introduced in Section III) and the above-stated permittivity estimation procedure were used. For each case, the errors between the estimated values $\Re(\tilde{\varepsilon}_r)$, $\Im(\tilde{\varepsilon}_r)$ and the true values $\Re(\varepsilon_r)$ and $\Im(\varepsilon_r)$ were calculated as follows:

$$e_r = \frac{\Re(\tilde{\varepsilon}_r) - \Re(\varepsilon_r)}{\Re(\varepsilon_r) - 1}, \quad e_i = \frac{\Im(\tilde{\varepsilon}_r) - \Im(\varepsilon_r)}{\Im(\varepsilon_r)} \tag{17}$$

TABLE I
Errors for Lossy and Low-Loss Targets

Target permittivity	Max. e_r (%)	Max. e_i (%)
3-3j	5.2	6.2
3-1j	2.5	10.4
3-0.5j	2.5	10.8
3-0.25j	3.0	23.0
3-0.1j	3.5	54.0

TABLE II
Errors for Strongly and Weakly Scattering Targets

Target permittivity	Max. e_r (%)	Signal strength (dB)
5–0.001j	2.8	–15
4–0.001j	4.2	–16
3–0.001j	3.3	–18
2–0.001j	5.4	–22
1.5–0.001j	6.4	–27
1.25–0.001j	16	–33
1.1–0.001j	14	–41
1.05–0.001j	68	–47
1.01–0.001j	670	–60

and the largest error across the 15 frequencies was identified. The first test involved investigating the algorithm's ability to measure low-loss samples by obtaining the maximum measurement errors for a bloc of $\varepsilon = 3 - 3j$ (frequency invariant) and progressively reducing the loss (see Table I). The results show the technique to be reliable in regards to $\Re(\varepsilon_r)$ but a progressively increasing error in $\Im(\varepsilon_r)$ as it decreases. As the proposed technique is of the reflection type this behavior is to be expected. This is because the reflection off of a low-loss object is affected predominately by the real part of its permittivity with transmission measurements (of a significant sample length) required to establish a significant effect from the object's low loss [7], [40]. The next test involved investigating the algorithm's susceptibility to the strength of the OUT's return. This was done by setting the bloc to have a large contrast of $\varepsilon = 5 - 0.001j$ and slowly decreasing $\Re(\varepsilon_r)$ while noting the magnitude of the target's response (in dB and with reference to the free-space antenna's response) as well as the largest e_r in each frequency sweep. The results are in Table II and show that reliable measurements are made of $\Re(\varepsilon_r)$ for even relatively small contrasts. It also shows that measurement becomes unreliable for weak scatterers when their return strengths approach the noise floor (60 dB in this case).

The last synthetic test involved changing the target shape to a more obscure form. In this case, a 200-mL paper cup filled with isopropanol was simulated. This paper was assumed invisible to microwave radiation, while the complex permittivity of the isopropanol was obtained from [41]. The same calibration procedure was used as for the dielectric bloc and the cup was viewed side on and scanned through the same positions as the bloc. The mesh of the cup is shown in Fig. 3, while the resulting permittivity estimates are shown in Fig. 4. The maximum error in ε was 7.5%, showing that the technique is capable of operating on arbitrary shaped samples provided that the sample shape is known.

This verifies the material characterization and thus the antenna calibration against simulated data. However, the differences between the simulation of a scattering experiment and the real-world system are usually unknown and thus difficult

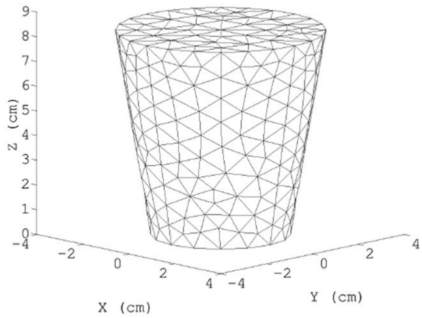

Fig. 3. Mesh of isopropanol filled cup.

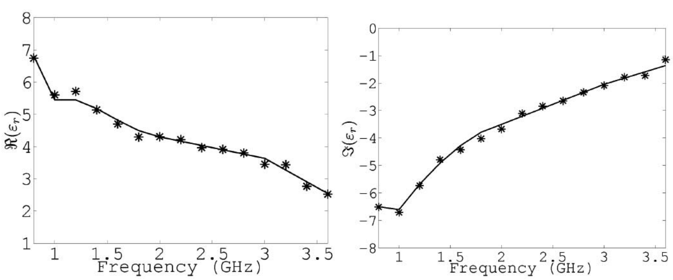

Fig. 4. Correct (solid lines) and measured (*) $\Re(\varepsilon_r)$ (left) and $\Im(\varepsilon)$ (right) for a 200-mL cup of isopropanol.

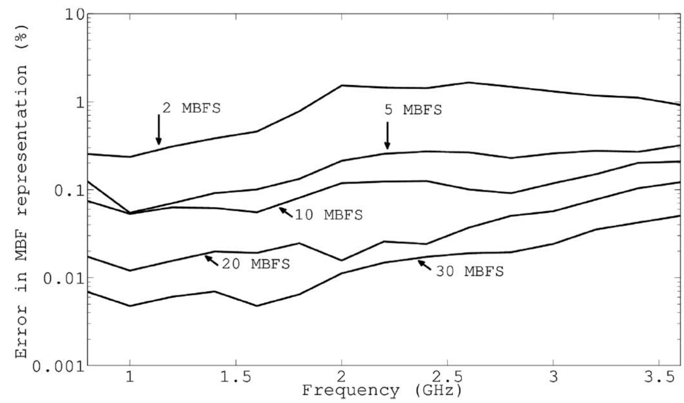

Fig. 5. RMS error in MBF representation of antenna's-induced current densities due to dielectric target, using 2, 5, 10, 20, and 30 MBFs.

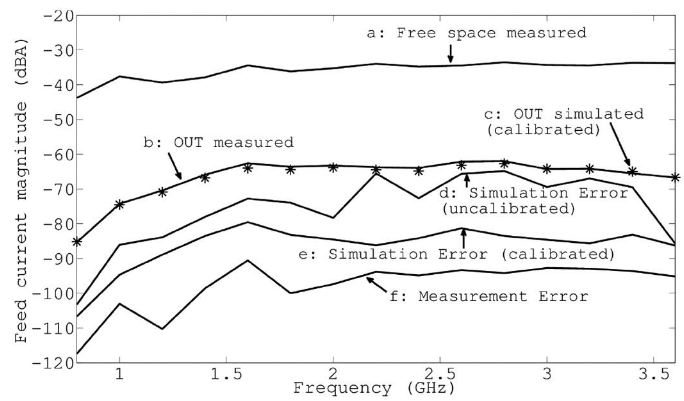

Fig. 6. Absolute value of feed currents. (a) Measured free space. (b) Measured difference current with OUT present (i.e., magnitude of OUT's contribution). (c,*) Simulated, calibrated difference current with OUT present (i.e., simulated magnitude of OUT's contribution with calibration). (d) Absolute value of error between complex uncalibrated simulation and measurement. (e) Absolute value of error between complex calibrated simulation and measurement. (f) Estimation of level of measurement error.

to approximate in software. Section V uses the experimental data to verify the functionality of the calibration method and subsequently the material estimation technique.

V. Experimental Results

This section presents detailed experimental results. It verifies the MBF selection procedure that provides accurate simulations of the antenna's feed current in the presence of the dielectric bloc from Neltec and presents precise measurements of the bloc's complex permittivity.

A conservative threshold of 10^5 was allowed between the largest and smallest singular values when selecting the number of MBFs. This led to the use of $12 \leq M \leq 35$ MBFs with higher frequencies requiring more than lower frequencies. Note that this enabled a considerable computational cost reduction as $N = 1585$. The accuracy of the MBF representation was tested. To do this, (1) was used to calculate the current density vector across the antenna in the presence of the test dielectric ($\boldsymbol{x}_1^{\mathrm{diel}}$) and in free-space ($\boldsymbol{x}_1^{\mathrm{fs}}$). Subtracting these two values gave the OUT's contribution to the antenna current density

$$\Delta \boldsymbol{x}_1 = \boldsymbol{x}_1^{\mathrm{diel}} - \boldsymbol{x}_1^{\mathrm{fs}}. \tag{18}$$

The ability, of the MBF reduced system of equations to represent the problem at hand, was then tested by calculating the percentage RMS error between $\Delta \boldsymbol{x}_1$ and its MBF representation as

$$100 \frac{||\Delta \boldsymbol{x}_1 - \boldsymbol{Q}\boldsymbol{Q}^H \Delta \boldsymbol{x}_1||^2}{||\Delta \boldsymbol{x}_1||^2} \tag{19}$$

where $||\cdots||^2 = \sqrt{\sum |\cdots|^2}$ is the Frobenius norm and ^{H} indicates the Hermitian transpose. Fig. 5 plots (19) as a function of frequency and the number of MBFs used. Thus, showing that while a very few MBFs were used to obtain the results in this paper, a significantly smaller number would be sufficient.

A direct test of the accuracy of the calibration procedure was performed by comparing the measured feed currents with the calibrated and uncalibrated simulations. Fig. 6 plots the magnitude of the measured feed current in the absence of an OUT (i.e., free space), the measured and simulated difference currents in the presence of the dielectric target (i.e., the magnitude of the OUT's contribution), and the magnitudes of the complex errors between the simulations and measurements. Note that, while the simulated and measured phases are not directly compared, they are similar, as can be seen by the small value of the magnitude of the complex errors [see (d) and (e) in Fig. 6]. The rms error between the measured feed currents for symmetrically placed calibration targets is also given as an estimate of the measurement error. The close match between lines (b) and (c) and the significantly smaller value of line (e) compared to (d) clearly show that the calibration significantly improved the match between simulated and measured currents. This is further emphasized in Fig. 7 that plots the difference between

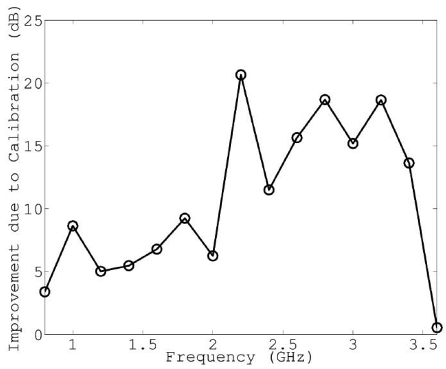

Fig. 7. Improvement due to calibration, i.e., difference between absolute errors in uncalibrated and calibrated simulations.

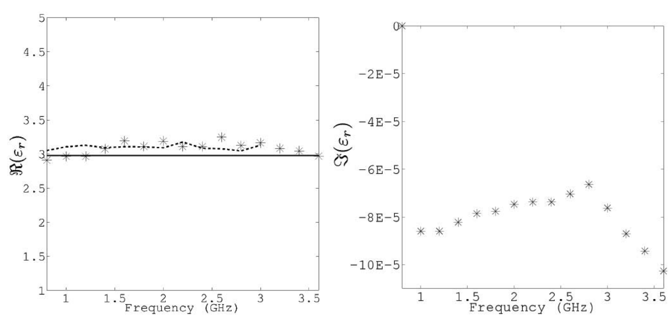

Fig. 8. Permitivitty measurement results. Left: manufacturer's stated $\Re(\varepsilon_r)$ (solid line), co-axial probe's measured $\Re(\varepsilon_r)$ (dashed line), and novel method's measured $\Re(\varepsilon_r)$ (*'s) . Right: novel method's measured $\Im(\varepsilon_r)$, manufacturer stated $|\Im(\varepsilon_r)| < 0.005$ (not plotted), and co-axial probe's measurement $\Im(\varepsilon_r) < 0.05$ (not plotted).

the absolute errors in uncalibrated and calibrated simulations and therefore the improvement obtained from calibration. A frequency-dependent improvement of between 2 and 21 dB was recorded. This frequency dependence is due to the MoM model being more accurate at some frequencies than others and the feed current being larger at certain frequencies. This demonstrates a very accurate simulation of the feed current, which is suitable for use in near-field sensing or imaging problems, including measuring constitutive parameters. The complex permittivity was then estimated using the inversion procedure in Section II-C. The results are presented in Fig. 8, along with the manufacturer's stated frequency stable complex permittivity of $\Re(\varepsilon_r) = 2.98$ and $|\Im(\varepsilon_r)| < 0.005$ and the contact probe's permittivity measurements. Note that, the contact probe used is limited to an upper frequency of 3 GHz and is not sensitive to loss tangents below 0.05 ($|\Im(\varepsilon_r)| < 0.15$). This figure shows a maximum error in $\Re(\varepsilon_r)$ of 5% (at 2.6 GHz) and satisfies the manufacturer's claimed $|\Im(\varepsilon_r)| < 0.005$. The contact probe's measurements of $|\Im(\varepsilon_r)|$ were all below 0.05, verifying that the true value is below the apparatus's sensitivity. Note, as the proposed method performs a reflection measurement, it is not expected to give accurate estimates of the loss of extremely low-loss materials such as the OUT in question. See Table I for an indication of the technique's sensitivity to low-loss values.

VI. Discussion

For the tests in this paper, no false minimums were present when inverting for the constitutive parameters. This does not guarantee that other OUTs will not exhibit multiple minimums in (16). The probability of such occurrences may be decreased by increasing D, the number of positions/orientations of the OUT, thus increasing the data to unknowns' ratio.

A very simple setup was used where the OUT was simply moved through numerous positions in the near field of a single antenna. This approach has the advantages of simplicity and ease of operation. However, it may not prove sufficient for all possible applications of the calibration method. Other configurations may be considered, for example, using multiple antennas to obtain transmission measurements [42]. Reflectors could be used to increase the return from electrically small OUTs.

Only small errors are present in the MBF representation even when as little as two MBFs are used (see Fig. 5). This occurs as only sources in the set of directions covered by the calibration target positions need to be accurately represented. Indeed, when the OUT is placed significantly outside the set of calibrated directions, (5) may give large errors.

It is important to achieve accurate positioning of the OUTs and the probing antenna. This was done by hand for the experiments in this paper (estimated positioning accuracy of 2 mm, note the antenna and target meshes are significantly more accurate). However, mechanical scanners may be used if they do not perturb the near-field responses of the antenna or OUT.

The authors' intended application of the calibration technique is to develop a method of characterizing dielectric samples whose shape, size, or surface roughness does not allow nondestructive characterization via traditional methods (e.g., waveguides, co-axial probes, etc.). However, the calibration may be applied to a large range of near-field problems.

An interesting extension to this work would be to apply it to the related problem of soil permittivity measurement with the use of a GPR [12], [19], [30], [43]–[45]. The main interest being that the GPR problem typically uses a less accurate dipole or transmission line equivalent representation of the antennas [19], [30], [43]. The proposed extension would require the use of planarly layered Green's functions and thus represents a deviation from the formulation presented above [46].

The proposed calibration technique has links to the well known and still largely unsolved problem of microwave tomography where the map of the inhomogeneous intrinsic parameters of an OUT is obtained from detailed measurements of its scattered field via an ill-posed inverse problem [1]–[4]. However, for the problem at hand, the object is known in advance to have a given shape and to be homogeneous (thus, the authors' problem is better posed). The problem at hand also requires a more precise parameter estimation, while tomography is typically concerned with image formation and the distinction of different regions, thus more significant errors in intrinsic parameter values are usually accepted [1]–[4]. The calibration technique proposed in this paper, or one similar to it, might also find application in tomography techniques.

VII. Conclusion

A novel calibration procedure has been presented, which enables for accurate (full wave) representation of antennas in the forward scattering component of near-field inverse problems. The experimental procedure is simple to perform and involves measuring the S_{11} parameter of an antenna first in the presence of a near-field calibration target and then of the OUT. MoM simulations are performed of the calibration target/antenna system and the induced current densities on the probing antenna used. With these current densities, MBFs are obtained that accurately represent fields' incident from the direction of the calibration target (and later the OUT). This MBF selection process allows for a significant reduction in the computational cost due to the antenna–antenna and antenna–OUT interactions. A small set of parameters is then introduced, which alters the MBFs used to represent the antenna current densities. The calibration sets these parameters by minimizing the RMS error between the measured and MoM simulated antenna feed currents obtained in the presence of the calibration target. This caters for unknown differences between the MoM system model and the real-world instrument. The use of the recently developed FMIR–MoM technique allows one to efficiently change the constitutive parameters and frequency when simulating the OUT, and thus the calibrated system model may be efficiently applied to the problem of material characterization.

The calibration method has been verified by applying it to the problem of estimating dielectric parameters of OUTs of known but arbitrary shape. Extensive results on both simulated and experimental data show that the calibration method:

1) accurately caters for antenna–antenna and antenna–OUT interactions with negligible additional computational cost;
2) corrects for small differences between the simulation model and the real-world system (e.g., modeling errors, mounting and pointing errors, etc.); and
3) allows for accurate estimation of material dielectric properties for samples of known but otherwise arbitrary shape.

References

[1] K. Belkebir and M. Saillard, "Guest editors introduction: Testing inversion algorithms against experimental data: Inhomogeneous targets," *Inverse Prob.*, vol. 21, pp. s1–s3, 2005.

[2] A. Abubakar, P. van den Berg, and T. Habashy, "Application of the multiplicative regularized contrast source inversion method on TM- and TE-polarized experimental Fresnel data," *Inverse Prob.*, vol. 21, pp. s5–s13, 2005.

[3] E. Kilic, F. Akleman, B. Esen, D. Ozaltin, O. Ozdemir, and A. Yapar, "3-D imaging of inhomogeneous materials loaded in a rectangular waveguide," *IEEE Trans. Microw. Theory Techn.*, vol. 58, no. 5, pp. 1290–1296, May 2010.

[4] C. Gilmore, P. Mojabi, and J. LoVetri, "Comparison of an enhanced distorted born iterative method and the multiplicative-regularized contrast source inversion method," *IEEE Trans. Antennas Propag.*, vol. 57, no. 8, pp. 2341–2351, Aug. 2009.

[5] L. van Kempen, H. D. Nho, H. Sahli, G. Hislop, and T. Tang, "A comparison of GPR reconstruction techniques," in *Proc. Tenth International Conference on Ground Penetrating Radar (GPR)*, 2004, vol. 1, pp. 345–348.

[6] O. Franza, N. Joachimowicz, and J.-C. Bolomey, "SICS: A sensor interaction compensation scheme for microwave imaging," *IEEE Trans. Antennas Propag.*, vol. 50, no. 2, pp. 211–216, Feb. 2002.

[7] L. Chen, C. Ong, C. Neo, V. V. Varadan, and V. K. Varadan, *Microwave Electronics and Materials Characterization*. Hoboken, NJ, USA: Wiley, 2004.

[8] K. Rajab, K.-F. Fuh, R. Mittra, and M. Lanagan, "Dielectric property measurement using a resonant nonradiative dielectric waveguide structure," *IEEE Microw. Wireless Compon. Lett.*, vol. 15, no. 2, pp. 104–106, Feb. 2005.

[9] T. Iglesias and S. Pereira, "Distributed parameters for low-frequency dielectric characterization of liquids with open-ended coaxial cell," *IEEE Trans. Instrum. Meas.*, vol. 55, no. 1, pp. 176–179, Feb. 2006.

[10] G. Hislop, "Measuring the thickness, permittivity and conductivity of layered earth," in *Proc. 8th Eur. Conf. Antennas Propag. (EUCAP)*, Apr. 2014, pp. 4367–4370.

[11] G. Hislop and C. Craeye, "Permittivity measurement under free space propagation," in *Proc. 6th Eur. Conf. Antennas Propag. (EUCAP)*, Mar. 2012, pp. 3509–3512.

[12] G. Hislop, "Limitations of characterizing layered earth with off-ground GPR," *J. Geophys. Eng.*, 2016, to be published.

[13] C. Yu et al., "Active microwave imaging II: 3-D system prototype and image reconstruction from experimental data," *IEEE Trans. Microw. Theory Techn.*, vol. 56, no. 4, pp. 991–1000, Apr. 2008.

[14] A. Bulyshev et al., "Computational modeling of three-dimensional microwave tomography of breast cancer," *IEEE Trans. Biomed. Eng.*, vol. 48, no. 9, pp. 1053–1056, Sep. 2001.

[15] A. Hassan and M. El-Shenawee, "Review of electromagnetic techniques for breast cancer detection," *IEEE Trans. Biomed. Eng.*, vol. 4, pp. 103–118, Sept. 2011.

[16] T. Henriksson, N. Joachimowicz, C. Conessa, and J.-C. Bolomey, "Quantitative microwave imaging for breast cancer detection using a planar 2.45 GHz system," *IEEE Trans. Instrum. Meas.*, vol. 59, no. 10, pp. 2691–2699, Oct. 2010.

[17] E. Attardo, A. Borsic, G. Vecchi, and P. Meaney, "Whole-system electromagnetic modeling for microwave tomography," *IEEE Antennas Wireless Propag. Lett.*, vol. 11, pp. 1618–1621, 2012.

[18] M. Klemm, J. Leendertz, D. Gibbins, I. Craddock, A. Preece, and R. Benjamin, "Microwave radar-based breast cancer detection: Imaging in inhomogeneous breast phantoms," *IEEE Antennas Wireless Propag. Lett.*, vol. 8, pp. 1349–1352, Nov. 2009.

[19] S. Lambot, E. Slob, I. van den Bosch, B. Stockbroeckx, and M. Vanclooster, "Modeling of ground-penetrating radar for accurate characterization of subsurface electric properties," *IEEE Trans. Geosci. Remote Sens.*, vol. 42, no. 11, pp. 2555–2568, Nov. 2004.

[20] M. Ostadrahimi et al., "Analysis of incident field modeling and incident/scattered field calibration techniques in microwave tomography," *IEEE Antennas Wireless Propag. Lett.*, vol. 10, pp. 900–903, Sep. 2011.

[21] R. Amineh, J. McCombe, A. Khalatpour, and N. Nikolova, "Microwave holography using point-spread functions measured with calibration objects," *IEEE Trans. Instrum. Meas.*, vol. 64, no. 2, pp. 403–417, Feb. 2015.

[22] L. Bellomo, S. Pioch, M. Saillard, and K. Belkebir, "An improved antenna calibration methodology for microwave diffraction tomography in limited-aspect configurations," *IEEE Trans. Antennas Propag.*, vol. 62, no. 5, pp. 2450–2462, May 2014.

[23] S. M. Rao and D. R. Wilton, "E-field, H-field, and combined field solution for arbitrarily shaped three-dimensional dielectric bodies," *Electromagnetics*, vol. 10, no. 4, pp. 407–421, 1990.

[24] P. Yla-Oijala, M. Taskinen, and J. Sarvas, "Surface integral equation method for general composite metallic and dielectric structures with junctions," *Progr. Electromagn. Res.*, vol. 52, pp. 81–108, 2005.

[25] D. Wilton, "Computational methods," in *Scattering: Scattering and Inverse Scattering in Pure and Applied Science*, E. R. Pike and P. C. Sabatier, Eds. New York, NY, USA: Academic Press/Elsevier, 2002, pp. 316–365.

[26] G. Hislop, N. A. Ozdemir, C. Craeye, and D. González-Ovejero, "MoM matrix generation based on frequency and material independent reactions (FMIR-MoM)," *IEEE Trans. Antennas Propag.*, vol. 60, no. 12, pp. 5777–5786, Dec. 2012.

[27] E. Suter and J. R. Mosig, "A subdomain multilevel approach for the efficient MoM analysis of large planar antennas," *Microw. Opt. Technol. Lett.*, vol. 26, pp. 270–277, Mar. 2000.

[28] V. V. S. Prakash and R. Mittra, "Characteristic basis function method: A new technique for efficient solution of method of moments matrix equations," *Microw. Opt. Technol. Lett.*, vol. 36, no. 2, pp. 95–100, 2003.

[29] C. Craeye, "A fast impedance and pattern computation scheme for finite antenna arrays," *IEEE Trans. Antennas Propag.*, vol. 54, no. 10, pp. 3030–3034, Oct. 2006.

[30] G. Hislop, S. Lambot, C. Craeye, D. Gonzalez-Ovejero, and R. Sarkis, “Antenna calibration for near-field problems with the method of moments,” in *Proc. 5th Eur. Conf. Antennas Propag. (EUCAP)*, Apr. 2011, pp. 2004–2008.

[31] S. Rao, D. Wilton, and A. Glisson, “Electromagnetic scattering by surfaces of arbitrary shape,” *IEEE Trans. Antennas Propag.*, vol. AP-30, no. 3, pp. 409–418, May 1982.

[32] D. Pozar, *Microwave Engineering*, 2nd ed. Hoboken, NJ, USA: Wiley, 1998.

[33] L. Matekovits, V. A. Laza, and G. Vecchi, “Analysis of large complex structures with the synthetic-functions approach,” *IEEE Trans. Antennas Propag.*, vol. 55, no. 9, pp. 2509–2521, Sep. 2007.

[34] R. Maaskant, R. Mittra, and A. Tijhuis, “Fast analysis of large antenna arrays using the characteristic basis function method and the adaptive cross approximation algorithm,” *IEEE Trans. Antennas Propag.*, vol. 56, no. 11, pp. 3440–3451, Nov. 2008.

[35] G. Hislop and C. Craeye, “An accelerated implementation of the FMIR-MoM algorithm,” in *Proc. 7th Eur. Conf. Antennas Propag. (EuCAP)*, Apr. 2013, pp. 202–206.

[36] J. C. Lagarias, J. A. Reeds, M. H. Wright, and P. E. Wright, “Convergence properties of the Nelder–Mead simplex method in low dimensions,” *SIAM J. Optim.*, vol. 9, no. 1, pp. 112–147, 1998.

[37] R. Sarkis and C. Craeye, “Circular array of wideband 3D Vivaldi antennas,” in *Proc. Int. Symp. Electromagn. Theory (EMTS)*, Aug. 2010, pp. 792–794.

[38] A. Bhattacharya, R. Sarkis, G. Hislop, S. Lambot, and C. Craeye, “Modeling of an ultra-wideband antenna array devoted to near-field imaging,” in *Proc. Loughborough Antennas Propag. Conf. (LAPC)*, Nov. 2010, pp. 545–548.

[39] A. Wirgin, “The inverse crime,” 2004, *arXiv preprint math-ph/0401050*.

[40] D. D. J. Baker-Jarvis and M. Janezic, “High-frequency dielectric measurements,” *IEEE Instrum. Meas. Mag.*, vol. 13, no. 2, pp. 24–31, Apr. 2010.

[41] J. Wosik, J. Miller, D. S. McKay, D. Warmflash, and M. Kamel, “High-frequency dielectric spectroscopy for martian soil samples,” *Proc. Inst. Space Syst. Oper.*, 2004, pp. 114–118.

[42] K. Alkhalifeh, R. Sarkis, and C. Craeye, “Design of a novel 3D circular Vivaldi antennas array for ultra-wideband near-field radar imaging,” in *Proc. 6th Eur. Conf. Antennas Propag. (EUCAP)*, Mar. 2012, pp. 898–901.

[43] S. Lambot and F. Andre, “Full-wave modeling of near-field radar data for planar layered media reconstruction,” *IEEE Trans. Geosci. Remote Sens.*, vol. 52, no. 5, pp. 2295–2303, May 2014.

[44] G. Hislop, “Ground permittivity estimation using radar to ground coupling,” in *Proc. 9th Eur. Conf. Antennas Propag. (EUCAP)*, Apr. 2015.

[45] G. Hislop, “Permittivity estimation using coupling of commercial ground penetrating radars,” *IEEE Trans. Geosci. Remote Sens.*, vol. 53, no. 8, pp. 4157–4164, Aug. 2015.

[46] K. Alkhalifeh, N. Ozdemir, and C. Craeye, “Efficient simulation of coupled ground antennas,” in *Proc. 9th Eur. Conf. Antennas Propag. (EUCAP)*, Apr. 2015.

Greg Hislop (M’06–SM’15) was born in Australia in 1978. He received the Bachelor’s degree in electrical and electronic engineering and the Ph.D. degree in inverse scattering techniques for the imaging of shallowly buried objects with ground penetrating radar from the Queensland University of Technology, Brisbane, Australia, in 2000 and 2006, respectively.

From 2005 to 2008, he was with the CSIRO’s ICT Centre, Sydney, Australia. In this position, he worked on the application of phase retrieval techniques to THz imaging applications as well as the detection of faults in the trunks of plantation pines using radar. From 2009 to August 2012, he worked on the direction of arrival finding techniques, novel permittivity measurement methods, and electromagnetic simulation algorithms at the Université catholique de Louvain, Louvain-la-Neuve, Belgium. From 2012 till late 2015, he was a Research Scientist with the Energy Flagship, CSIRO, Brisbane, QLD, Australia, where he focused on mining applications for radar. Since 2016, he has been an Algorithmic Specialist with Fugro-Roames, Brisbane, Australia.

Dr. Hislop was the Vice Chair and Chair of the IEEE MTT/AP Chapter within the Queensland Section, in 2014 and 2015, respectively.

Christophe Craeye (M’98–SM’11) was born in Belgium in 1971. He received the Electrical Engineering and Bachelor in Philosophy degrees and the Ph.D. degree in applied sciences from the Universit catholique de Louvain (UCL), Louvain-la-Neuve, Belgium, in 1994 and 1998, respectively.

From 1994 to 1999, he was a Teaching Assistant with UCL and carried out research on the radar signature of the sea surface perturbed by rain, in collaboration with NASA and ESA. From 1999 to 2001, he was a Postdoctoral Researcher with the Eindhoven University of Technology, Eindhoven, The Netherlands. His research there was related to wideband phased arrays devoted to the square kilometer array radio telescope. In this framework, he was also with the University of Massachusetts, Amherst, MA, USA, in the Fall of 1999, and was with the Netherlands Institute for Research in Astronomy, Dwingeloo, The Netherlands, in 2001. In 2002, he started an antenna research activity at the Universit catholique de Louvain, where he is now a Professor. He was with the Astrophysics and Detectors Group, University of Cambridge, Cambridge, U.K., from January to August 2011. His research is funded by Région Wallonne, European Commission, FNRS, and UCL. His research interests include finite antenna arrays, wideband antennas, small antennas, metamaterials, and numerical methods for fields in periodic media, with applications to communication and sensing systems.

Prof. Craeye was an Associate Editor of the IEEE TRANSACTIONS ON ANTENNAS AND PROPAGATION from 2004 to 2010. He has been an Associate Editor of the *IEEE Antennas and Wireless Propagation Letters*. In 2009, he was the recipient of the 2005–2008 Georges Vanderlinden Prize from the Belgian Royal Academy of Sciences.

David González-Ovejero (S’01–M’13) was born in Gandía, Spain, in 1982. He received the Telecommunication Engineering degree from the Universidad Politécnica de Valencia, Valencia, Spain, in 2005, and the Ph.D. degree in electrical engineering from the Université catholique de Louvain, Louvain-la-Neuve, Belgium, in 2012.

From January 2006 to September 2007, he was a Research Assistant with the Universidad Politécnica de Valencia. In October 2007, he was a Research Assistant with the Université catholique de Louvain, until October 2012. From November 2012 to October 2014, he was a Research Associate with the University of Siena, Siena, Italy. Since November 2014, he has been a Marie Curie Postdoctoral Fellow with the Jet Propulsion Laboratory, California Institute of Technology, Pasadena, CA, USA. His research interests include the fields of computational electromagnetics, the analysis and design of antenna arrays, and metasurfaces.